ACS Photonics

Open Access

pubs.acs.org/journal/apchd5

Article

Dielectric Tetramer Nanoresonators Supporting Strong Superchiral Fields for Vibrational Circular Dichroism Spectroscopy

Longfang Ye, Jingyan Li, Felix Ulrich Richter, Yasaman Jahani, Rui Lu, Bo Ray Lee, Ming Lun Tseng,* and Hatice Altug*

Cite This: *ACS Photonics* 2023, 10, 4377–4384

Read Online

ACCESS | Metrics & More | Article Recommendations | Supporting Information

ABSTRACT: Chirality (C) is a fundamental property of objects, in terms of symmetry. It is extremely important to sense and distinguish chiral molecules in the fields of biochemistry, science, and medicine. Vibrational circular dichroism (VCD) spectroscopy, obtained from the differential absorption of left- and right- circularly polarized light (CPL) in the infrared range, is a promising technique for enantiomeric detection and separation. However, VCD signals are typically very weak for most small molecules. Dielectric metasurfaces are an emerging platform to enhance the sensitivity of VCD spectroscopy of chiral molecules via superchiral field manipulation. Here, we demonstrate a dielectric metasurface consisting of achiral germanium (Ge) tetramer nanoresonators that provide a proper and accessible high C enhancement (C_E). We realize a maximum C enhancement (C_{E_max}) with respect to the incident CPL ($C_{E\_max} = C_{max}/C_{RCP}$) of more than 750. The volume-averaged C enhancement ($C_{E\_ave} = C_{ave}/C_{RCP}$) is 148 in the 50 nm thick region above the sample surface and 215 in the central region of the structure. Especially, the corresponding C_{E_ave} values are more than 89 and 183 even when a 50 nm thick chiral lossy molecular layer is coated on the metasurface. The metasurface benefits from geometrically achiral nanostructure design to eliminate intrinsic background chiral-optical signal from the substrate, which is useful in chiral sensing, enantioselectivity, and VCD spectroscopy applications in the mid-infrared range.

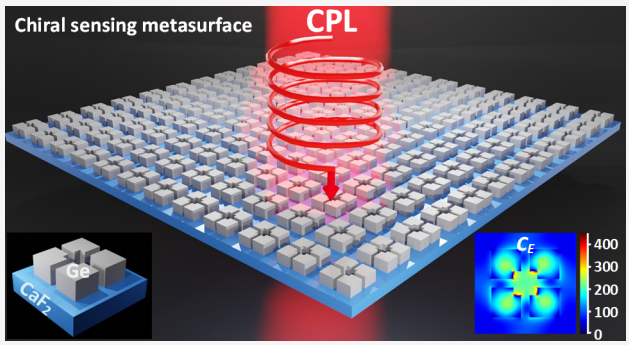

KEYWORDS: *optical chirality, mid-infrared, dielectric metasurface, nanoresonator, vibrational circular dichroism (VCD), chiral sensing*

INTRODUCTION

Chirality is a fundamental property of objects in terms of symmetry that plays an important role in biological systems.[1] An object is chiral if it cannot coincide with its mirror image.[2−4] Many biomolecules and drugs such as amino acids, glucose, proteins, carbohydrates, limonene, sugar, camphor, and thalidomide are chiral molecules that can be divided into left (*sinister*, *s*-) and right (*dexter*, *d*-) enantiomers. The chiral absorption responses of most biomolecules are located in the infrared, visible, and ultraviolet range.[5−9] The properties of chiral molecules can be greatly dependent on their chirality even though they have indistinguishable properties in molecular weight, density, transition frequency, etc. For example, left-handed thalidomide is an effective sedative, while right-handed thalidomide is a teratogen. The misuse of right-handed thalidomide led to thousands of children with severe birth defects.[10] Most biological molecules, such as amino acids, are chiral. Many chiral proteins containing D-amino acids may greatly impact human health and disease. The proteins β-amyloid, elastin, and α-crystallin play an important role in Alzheimer's disease, arteriosclerosis, and cataracts.[11] Therefore, it is extremely important to distinguish the molecule chirality in the fields of analytical biochemistry, science, food industry, and medicine.[12−14] Circular dichroism (CD) spectroscopy, calculated from the differential absorption spectra of left-handed (LCP) and right-handed (RCP) circularly polarized light (CPL) incidence, is a traditional technique widely used for chiral enantiomeric detection and separation.[15] Vibrational circular dichroism (VCD) spectroscopy is the CD spectroscopy counterpart in the mid-infrared range, and it is an equally useful technique for determining the structure and enantiomeric purity of chiral molecules and species.[16,17] Most of the critical pharmaceutical and biological molecules such as drugs, DNA, and proteins show VCD in the mid-IR range,[18−21] thus allowing simultaneous fingerprint identification of the bioanalytes and their chirality. However, owing to the low chiral-optical response, the CD signals of

Received: August 18, 2023
Revised: October 15, 2023
Accepted: October 20, 2023
Published: November 8, 2023

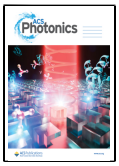

https://doi.org/10.1021/acsphotonics.3c01186
ACS Photonics 2023, 10, 4377−4384

most chiral molecules are small, typically 10^{-3} to 10^{-6}[17,22] in the ultraviolet range. The VCD signals in the mid-infrared are extremely weak, around 3 orders of magnitude smaller than those in the ultraviolet.[16,17] Therefore, high-sensitivity VCD spectroscopy is an ongoing challenge.

Recently, metasurfaces have provided new means for enhancing the sensitivity of photonics biosensing technologies.[23−25] Metasurfaces are photonic structures consisting of subwavelength nanoantennas as resonant unit cells.[26−28] The capabilities of the strong resonances of a metasurface under illumination enable them to enhance the electromagnetic (EM) field surrounding them and thus improve the sensing performance.[23−27,29] Recently, it has been found that the weak CD signals of chiral molecules can also be increased significantly by metasurfaces supporting strong superchiral fields (with optical chirality, C, larger than CPL).[25] The enhancement of CD signals is proportional to the optical chirality of the nanophotonic structures. Plasmonic metasurfaces consisting of metallic nanoresonators can provide high superchiral near-fields and enhanced light−matter interactions for chiral molecules. For example, plasmonic nanostructures with metallic slits, helices, gammadions, spirals, etc., were proposed and engineered to achieve high optical chirality enhancement (maximum optical chirality enhancement, C_{E_max}, up to 2 orders) compared with CPL.[12,15,30−39] However, planar plasmonic nanostructures usually show nonuniform spatial distribution of superchiral fields with opposite handedness, restricting their volume-averaged optical chirality enhancement (C_{E_ave}).[38] Three-dimensional plasmonic metasurfaces can generate a uniform superchiral field on their surfaces, but multistep and complex processes are usually needed for their nanofabrication.[39] In addition, nanostructures based on chiral geometries induce intrinsic background chiral-optical signals, which constrain the reliable detection of weak signals of chiral molecules.

Achiral dielectric metasurfaces made of high-index dielectric materials have been found to be a promising alternative platform for chiral sensing via superchiral field manipulation under CPL illumination.[40−45] Compared to the planar plasmonic counterparts that only have electric resonances, dielectric metasurfaces not only support both electric and magnetic resonances but also have the advantages of smaller dissipation and lower thermal conductivity, offering higher C enhancement. For example, Mohammadi et al. proposed a Kerker-inspired dielectric metasurface based on a holey silicon disk array, which provides accessible superhelical near-fields in the holes with a volume-averaged optical chirality enhancement (C_{E_ave}) of 24 at visible frequencies.[44] To boost the C enhancement, Hu et al.[22] demonstrated a high-Q biperiodic diamond disk metasurface that provides single-sign optical chirality enhancement in the ultraviolet range. The highest localized C_{E_max} of 1130 and the C_{E_ave} of 100 on the 40 nm cut-plane above the metasurface are achieved when both the electric and magnetic dipole modes are spatially and spectrally overlapped. Yao and Zheng[2] presented the near-ultraviolet dielectric metasurface based on titanium dioxide nanocube dimers that can generate strong superchiral near-field hotspots in dimer gaps, showing a localized C_{E_max} of ∼370 and C_{E_ave} of 80 in the gaps. In addition to the CPL illumination, linearly polarized visible light has been also used for the excitation of silicon nanocylinder dimer metasurfaces to generate strongly localized superchiral hotspots in the gaps.[25,41] Despite the recent progress, most of the reported dielectric metasurfaces were mainly focused on near-infrared, visible, and ultraviolet regions, and the achieved C_{E_ave} values were still relatively low.[2,10,22,41−46] Superchiral fields generated from previously reported disk-based designs[22,47] mainly localize inside dielectric meta-atoms. This feature is not favorable for sensing applications, as it prevents the interaction between the superchiral field and the chiral molecules. Therefore, it is of critical importance to investigate new dielectric metasurfaces with high C_E for high-efficiency and high-sensitivity VCD spectroscopy in the mid-infrared region.

In this paper, we propose a dielectric metasurface consisting of achiral germanium (Ge) tetramer nanoresonators, which provides an accessible and high optical chirality enhancement (C_E) in the mid-infrared region. With strong magnetic quadrupole resonances, the proposed metasurface can produce strong and uniform localized superchiral hotspots around the inner corners of the nanoresonators. It is found that optical chirality can be increased by 2 orders of magnitude with a localized C_{E_max} of 750, $C_{E\_ave\_whole}$ of 148 in the 50 nm thick region above the sample surface, and $C_{E\_ave\_central}$ of 215 in the central region of the structure. Especially, the corresponding volume-averaged optical chirality enhancement ($C_{E\_ave\_bio} = C_{ave\_bio}/C_{RCP}$) is more than 89 ($C_{E\_ave\_whole\_bio}$) and 183 ($C_{E\_ave\_central\_bio}$) even when a 50 nm thick chiral molecule layer is homogeneously coated on the metasurface. Due to the significant optical chirality enhancement of the proposed design, our work provides a high-efficiency and high-sensitivity platform for ultrasensitive VCD spectroscopy.

METHODS

The relationship between the optical chirality, C, and the electromagnetic fields can be expressed as[22]

$$C = -\frac{\omega}{2c^2}\mathrm{Im}(\mathbf{E}^*\cdot\mathbf{H}) = -\frac{\omega}{2c^2}|\mathbf{E}||\mathbf{H}|\cos(\varphi_{\mathbf{iE,H}}) \tag{1}$$

where c and ω denote the speed and angular frequency of light, $\mathbf{E}$ and $\mathbf{H}$ are the electric and magnetic field vectors, and $\varphi_{iE,H}$ is the phase angle between $\mathbf{E}$ multiplied by the complex number i and $\mathbf{H}$, respectively. The simplest chiral light is CPL (RCP/+ and LCP/−) with $C_{CPL} = \pm\frac{\varepsilon_0\omega}{2c}E_0^2$, where E_0 (H_0) is the incident CPL electric (magnetic) field amplitude. Then, the localized optical chirality enhancement is defined as

$$C_E = \frac{C}{C_{RCP}} = -\frac{1}{c\varepsilon_0}\frac{|\mathbf{E}||\mathbf{H}|\cos(\varphi_{\mathbf{iE,H}})}{E_0^2} \tag{2}$$

According to eq 2, to obtain a metasurface design with high C_E, strong electric and magnetic fields overlapping spectrally and spatially as well as a $\pi/2$ phase shift are required.

Circular dichroism (CD) is calculated from the differential absorption of chiral molecules under the LCP/RCP incidence, which can be expressed as[47]

$$\mathrm{CD} \propto A^+ - A^- = -\frac{4}{\varepsilon_0}G''C \tag{3}$$

where A^+ and A^- represent the absorption of chiral molecules under RCP (+) and LCP (−) incidence, respectively, and G'' represents the chiral polarization rates of molecules. $A^\pm$ can be expressed as[47,48]

$$A^\pm = \frac{\omega}{2}(\alpha''|\mathbf{E}|^2 + \mu_0^2\chi''|\mathbf{H}|^2) \mp \frac{2}{\varepsilon_0}G''C \tag{4}$$

https://doi.org/10.1021/acsphotonics.3c01186
ACS Photonics 2023, 10, 4377−4384

where μ_0 and ε_0 represent the permittivity and permeability of the free space and α'' and χ'' represent the imaginary part of the molecule's electric polarizability and magnetic polarizability, respectively.

In addition, Kuhn's asymmetry factor g is used to describe the enantioselectivity of the system. When magnetic loss is negligible, g can be expressed as[46]

$$g = \frac{2(A^+ - A^-)}{A^+ + A^-} = -\left(\frac{G''}{\alpha''}\right)\left(\frac{8C}{\omega\varepsilon_0 |E|^2}\right) \quad (5)$$

For CPL, $g_{CPL} = -4G''/c\alpha''$. Then we can get the enhancements of Kuhn's dissymmetry factor as

$$g_E = \frac{g}{g_{CPL}} = \frac{2c}{\omega\varepsilon_0}\frac{C}{|\mathbf{E}|^2} \quad -\frac{1}{\omega c}\frac{|\mathbf{E}||\mathbf{H}|\cos(\varphi_{i\mathbf{E},\mathbf{H}})}{|\mathbf{E}|^2} \quad (6)$$

By considering eq 2, the higher C_E will be achieved when both the electric field amplitude (E) and magnetic field amplitude (H) increase, and their phase shift $\varphi_{i\mathbf{E},\mathbf{H}}$ is optimized. Equation 6 indicates that a higher g_E will be obtained when the E field amplitude is lower and the H field amplitude is higher, as well as with the optimized phase shift $\varphi_{i\mathbf{E},\mathbf{H}}$. Therefore, if a metasurface design can provide stronger magnetic resonance than electric resonance, then both C_E and g_E could be increased simultaneously, which is beneficial for increasing the chiral molecule detection sensitivity and recognition efficiency.

RESULTS AND DISCUSSION

Dielectric Metasurface with High Optical Chirality Enhancement. The schematic diagram of the proposed dielectric metasurface composed of an achiral Ge tetramer nanoresonator array arranged in a square lattice placed on a CaF_2 substrate is shown in Figure 1(a). The refractive indices of Ge and CaF_2 are 4.01 and 1.39, respectively. The CaF_2 substrate is transparent in the mid-infrared range. Figure 1(b) shows the unit cell of the metasurface with four Ge nanoresonators, where the period p = 4.581 μm, and the other parameters are set as a = 3.0682 μm, b = 1.0794 μm, h = 1.0275 μm, and g = 0.3901 μm. The advantages of this metasurface design are as follows. First, the Ge resonators can realize strong magnetic and electric field enhancement due to the Mie resonance. Second, enhanced uniform localized superchiral fields with high C_{E_ave} can be achieved inside the central hole and the gap areas, which are accessible to the chiral molecules surrounding the metasurface. Third, since the materials used for our metasurface design are almost dispersion-free in the mid-IR range, we can effectively adapt the design by scaling to target the desired chemicals in the experiment. In addition, to translate new sensing approaches into practical applications, an important consideration is the low-cost manufacturing of sensor chips. Given that the critical dimensions in our design exceed 300 nm, we expect them to be compatible with emerging wafer-scale nanofabrication processes such as deep ultraviolet (DUV) lithography and nanoimprinting.[29]

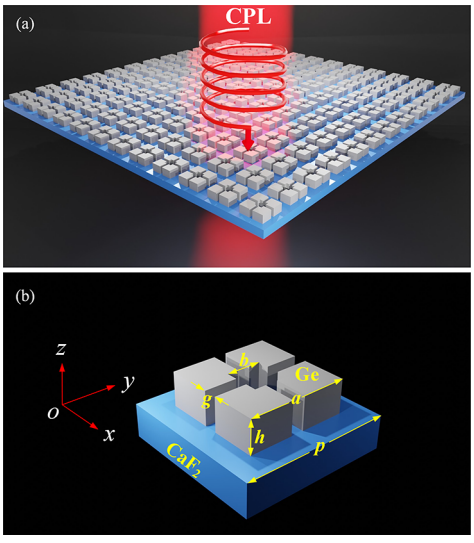

Figure 1. Schematic diagrams of the proposed dielectric metasurface (a) and its tetramer nanoresonator unit cell (b) illuminated by CPL. The parameters are set as a = 3.0682 μm, b = 1.0794 μm, h = 1.0275 μm, g = 0.3901 μm, and p = 4.581 μm.

To investigate the properties of the dielectric metasurface, we simulated its unit cell by using COMSOL Multiphysics, where periodic boundaries in both the x- and y-directions and symmetric meshes for the simulation models are assigned. Two ports are at the top and bottom of the structure for normal RCP incidence. Due to the relatively narrow bandwidth of the metasurface resonance, the wavelength range in the simulations was set from 6.48 to 6.66 μm. This setting enabled us to numerically investigate relevant metasurface properties efficiently. The transmittance (T) and reflectance (R) spectra of the dielectric metasurface under RCP illumination at 6.48–6.66 μm are shown in Figure 2(a). It is found that a peak transmittance of 0.97 and a minimum reflectance of 0.03 are achieved at 6.514 μm. At this wavelength, the transmittance approaches unity, implying that the dielectric metasurface satisfies a Kerker-like condition in which the handedness of the incident light is conserved.[22,40,47−49] The transmittance and reflectance spectra intersect with each other at 0.5 strength at two wavelengths of 6.524 and 6.552 μm. We use the multipole decomposition method to analyze the enhancement of electromagnetic fields caused by the Mie resonator.[50] It is accomplished by simulating the electric displacement current density in the metasurface and applying it to the formulas provided in ref 50. Multipole scattering cross-sectional areas of the electric dipole (ED), toroidal dipole (TD), magnetic dipole (MD), electric quadrupole (EQ), and magnetic quadrupole (MQ) of the metasurface are shown in Figure 2(b). It shows that the ED, TD, MD, EQ, and MQ have abrupt resonance peaks at around 6.524 μm, and the EQ and MQ have local maximums at around 6.514 μm. A detailed study of the Kerker coefficient (K_{RCP}) characterizing the metasurface's satisfaction of the generalized Kerker condition (yielding maximal forward scattering) is given in Section S1 of the Supporting Information. Figure 2(c) presents the calculated maximum enhancements of the electric and magnetic field amplitudes of the metasurface. The design supports high electric field amplitude enhancement (E/E_0) and magnetic field amplitude enhancement (H/H_0), exceeding 70 and 80 at around 6.514 μm, respectively. These high electromagnetic field enhancements provide the possibility of producing a large C value. Notably, at around 6.524 μm, both E/E_0 and H/H_0 show an abrupt peak, which also features spectrally overlapped multipolar resonance responses (Figure 2(b)). The calculated maximum C enhancement ($C_{E\_max} = C_{max}/C_{RCP}$) and minimum C enhancement ($C_{E\_min} = C_{min}/C_{RCP}$) in the entire simulation region are shown in Figure 2(d). It is found that at 6.514 and

https://doi.org/10.1021/acsphotonics.3c01186
ACS Photonics 2023, 10, 4377−4384

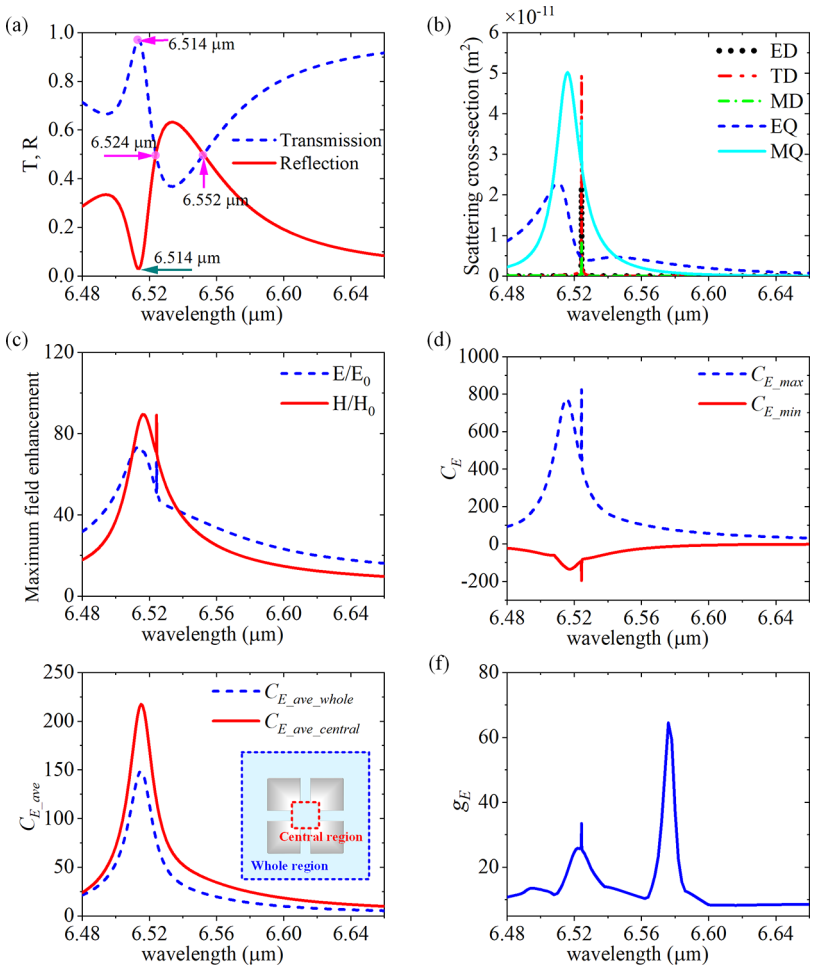

Figure 2. (a) The transmittance and reflectance spectra under normal RCP illumination. (b) Scattering spectra of ED, TD, MD, EQ, and MQ, respectively. (c) The calculated maximum enhancement of electric and magnetic field amplitude. (d) The maximum and minimum C_E in the whole structure. (e) The $C_{E\_ave\_whole}$ over a 50 nm homogeneous air layer upon the whole metasurface and $C_{E\_ave\_central}$ only in the central region of the structure. (f) Kuhn's dissymmetry factor enhancement (g_E). The pink arrows indicate the wavelengths.

6.517 μm the C_{E_max} peak of 750 and C_{E_min} dip of −135 can be achieved, respectively. Furthermore, to calculate volume-averaged C_{E_ave}, a 50 nm homogeneous thin air layer on the metasurface is chosen to be the calculation region. Figure 2(e) shows the $C_{E\_ave\_whole}$ for the 50 nm air layer above the metasurface and the $C_{E\_ave\_central}$ in the central region of the structure. It is found that the peak volume-averaged $C_{E\_ave\_whole}$ reaches 148, and $C_{E\_ave\_central}$ can get the maximum value of 215 at 6.514 μm, which is the highest volume-averaged C_E compared to the previously reported designs. Figure 2(f) shows Kuhn's dissymmetry factor enhancement g_E of the proposed metasurface. Notably, although abrupt peak values of C_{E_max} and g_E are achieved at around 6.524 μm, the volume-averaged C_E is not large at this point since the different signs of C are canceled out when taking the volume average in the thin layer volume area.

To better understand the mechanism of the optical chirality enhancement, we first plot the spatial distributions of the electric field amplitude enhancement (E/E_0), magnetic field amplitude enhancement (H/H_0), $\cos(\varphi_{iE,H})$, and the optical chirality enhancement (C_E) at the transmittance peak wavelength of 6.514 μm in the x−y plane at $z = h/2 = 0.51$ μm of the dielectric metasurface under normal RCP incidence in Figure 3, respectively. As shown in Figure 3(a), the enhanced electric fields are mainly distributed around the four inner edges and corners of the cut region of the Ge nanoresonators, and the maximum value of electric field enhancement can reach more than 40 in this cut plane. As shown in Figure 3(b), the enhanced magnetic fields are mainly located inside each Ge nanoresonator, and the maximum enhancement can reach more than 60 in this cut plane. Remarkably, both the enhanced electric and the magnetic fields (though not the peaks) overlap in space near the four cut corners and the hollow central region. Furthermore, Figure 3(c) shows the $\cos(\varphi_{iE,H})$ distribution at the $z = h/2$ cut plane region, indicating the phase difference between the electric and magnetic fields. The $\cos(\varphi_{iE,H})$ is generally negative for the entire cut plane region at 6.514 μm, which ensures that C_E is a positive value in that plane (according to eq 2), as shown in Figure 3(d). Therefore, the conditions for achieving high C_E (see the Methods section) are satisfied with this metasurface design. Figure 3(d) shows that the optical superchiral fields are mainly distributed around the inner corner of the four nanoresonators in the metasurface unit cell with the maximum C_E exceeding 300 in the cut plane. Furthermore, Figure 3(e) and (f) show the C_E cut on different planes (y = 1.27, 2.29, 3.31 μm and z = 0, 0.51, 1.02, 1.63 μm) of the dielectric metasurface at 6.514 μm. It is found that the C_E is generally positive on all cut planes, and especially a higher positive C_E can be achieved at lower cut planes close to the substrate surface. More analysis on the spatial distributions of

https://doi.org/10.1021/acsphotonics.3c01186
ACS Photonics 2023, 10, 4377−4384

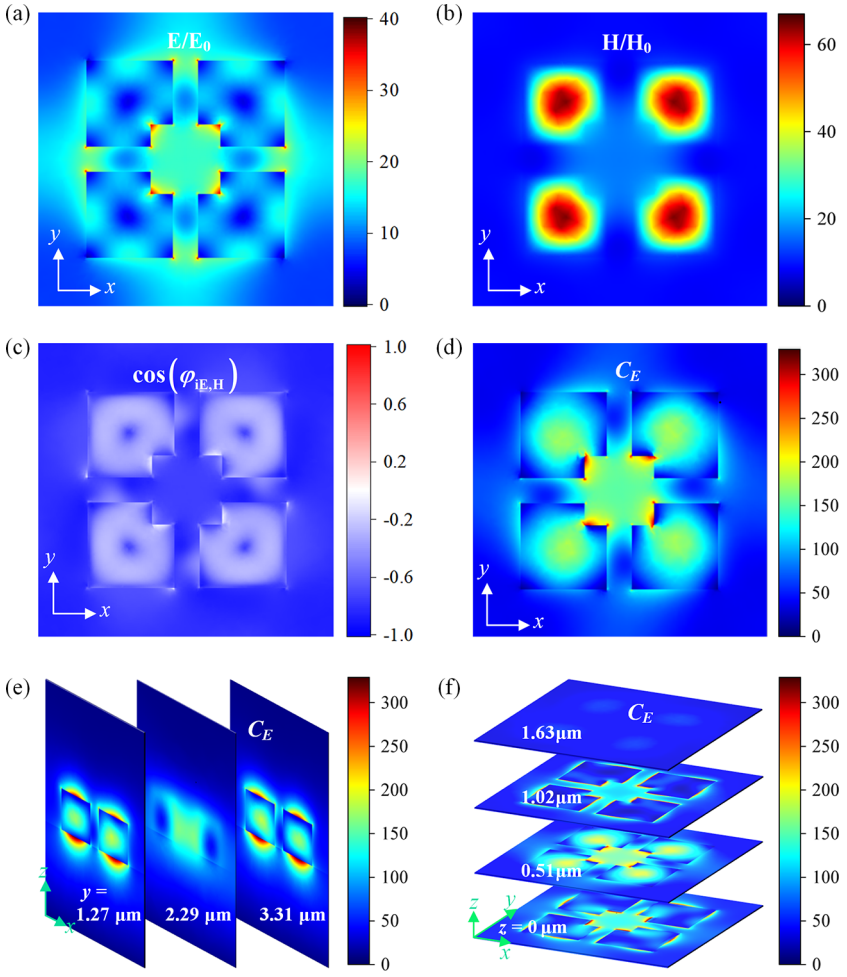

Figure 3. At the wavelength of 6.514 μm under normal RCP incidence, the distributions of (a) electric field amplitude enhancement E/E_0, (b) magnetic field amplitude enhancement H/H_0, (c) $\cos(\varphi_{iE,H})$, and (d) C_E cut on the $z = h/2 = 0.51$ μm plane of the dielectric metasurface. (e) C_E cut on different planes (y = 1.27, 2.29, 3.31 μm). (f) C_E cut on different cut planes (z = 0, 0.51, 1.02, and 1.63 μm).

the E/E_0, H/H_0, $\cos(\varphi_{iE,H})$, and C_E of the dielectric metasurface at the transmittance and reflectance intersection wavelengths of 6.524 and 6.552 μm can be found in Section S2 of the Supporting Information. Moreover, the impact of the geometric parameters of the tetramer nanoresonators on the C enhancement is further analyzed in Sections S3−S5 of the Supporting Information. The metasurface's resonance properties are observed to be robust to the sample fabrication imperfections.

Dielectric Metasurface for High-Sensitivity Chiral Sensing. To study the application of the reported metasurface for chiral sensing, we simulate its interaction with a thin biolayer. In the simulation, a 50 nm thick homogeneous chiral biolayer is coated uniformly on the entire dielectric metasurface, as shown in Figure 4(a). The Pasteur parameters and refractive indices of the chiral biomolecular layer are set as $\kappa = 0 + 0.001i$ and $n = 1.46-0.01i$,[44,51] respectively. The thickness and parameters of the chiral layer are set to be similar to the previous works.[44,51,52] To investigate the impact of the dielectric metasurface on VCD signal enhancement, we simulate the transmittance (T), reflectance (R), and absorption (A) of the metasurface with the chiral biolayer under normal RCP incidence. As shown in Figure 4(b), the T, R, and A of the metasurface with a biolayer at 6.61 μm are 0.711, 0.003, and 0.286, respectively. Compared with the T and R spectra

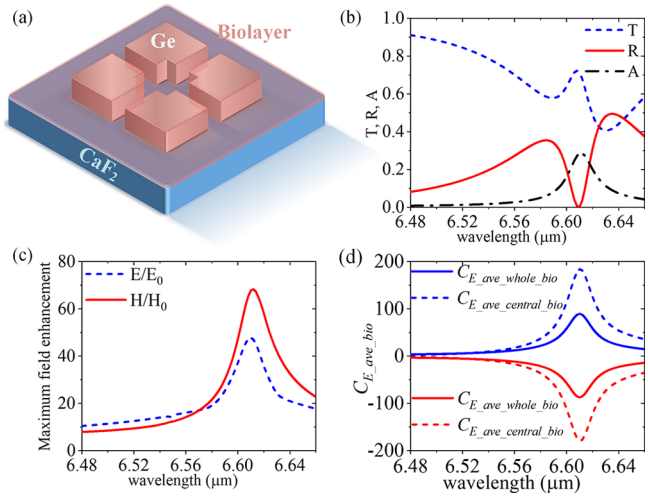

Figure 4. (a) Schematic diagram of the dielectric metasurface coated with a 50 nm homogeneous chiral biolayer. (b) T, R, and A of the metasurface with a biolayer under normal RCP incidence. (c) Maximum enhancement of electric (E/E_0) and magnetic (H/H_0) field amplitudes. (d) The $C_{E\_ave\_whole\_bio}$ (solid line) and $C_{E\_ave\_central\_bio}$ (dashed line) in biolayer volume above the metasurface under RCP (blue line) and LCP (red line) incidence.

https://doi.org/10.1021/acsphotonics.3c01186
ACS Photonics 2023, 10, 4377−4384

shown in Figure 2(a), an obvious red-shift of the spectra is observed when the biolayer is introduced, as shown in Figure 4(b). The calculated maximum enhancements of electric field amplitude E/E_0 and magnetic field amplitude H/H_0 for the metasurface with a biolayer are presented in Figure 4(c). High enhancements of electric and magnetic fields are obtained with peak values of 47.8 for E/E_0 and 68.3 for H/H_0 at around 6.61 μm. As shown in Figure 4(d), although the $C_{E\_ave\_whole}$ and $C_{E\_ave\_central}$ in the biolayer above the metasurface are lower than for the bare metasurface when averaged over the same volume (Figure 2(e)), at 6.61 μm under RCP illumination their peak still reaches 89 and 183, respectively. The impact of metasurface sample imperfection and material absorption on the $C_{E\_ave\_whole\_bio}$ and $C_{E\_ave\_central\_bio}$ is analyzed in Section S4 of the Supporting Information. It is found that our design is tolerant to fabrication imperfections (inner corner radius r up to 80 nm) and material absorption (Ge loss tangent up to 0.001). In addition, the dependence of the C enhancement on the Pasteur parameter κ (of different complex/real values and opposite signs) and thickness of the chiral biolayer is also discussed in Section S5 of the Supporting Information.

To further validate the effectiveness of the metasurface in chiral sensing, we sequentially illuminate the LCP and RCP on the metasurface with a 50 nm thick chiral biolayer under normal incidence. Considering the chiral biolayer is very thin ($\kappa\omega_0 \ll 1$), the differential transmittance for a bare chiral biolayer (without metasurface) between LCP and RCP can be expressed as $\Delta T = 4k_0\mathrm{Im}\{k\}\omega$. The enhancement of differential transmittance of the biological layer with and without the dielectric metasurface platform follows[43]

$$\frac{\Delta T^m}{\Delta T} = C_{E\_ave} \tag{7}$$

Figure 5(a) shows the simulated ΔT^m and ΔT for the metasurface with a biolayer and the biolayer only, respectively.

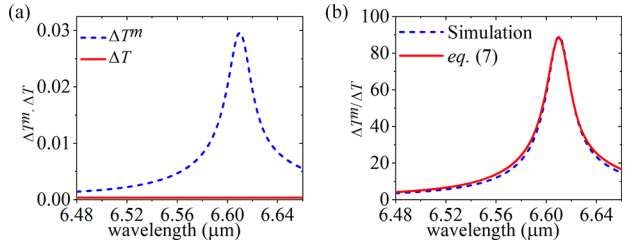

Figure 5. (a) Differential transmittance of the biolayer on the metasurface (blue) and of the same biolayer alone without a metasurface (red) between LCP and RCP. (b) Simulated $C_{E\_ave\_whole\_bio}$ (blue) and calculated $\Delta T^m/\Delta T$ (red).

The differential transmittance ΔT^m (of 0.0014−0.0297) for the metasurface with the biolayer is larger than the case of ΔT (of 0.00032−0.00034) for the biolayer alone, which can be predicted from the high $C_{E\_ave\_whole}$ of the proposed dielectric metasurface. The calculated $\Delta T^m/\Delta T$ and simulated $C_{E\_ave\_whole\_bio}$ are presented and compared in Figure 5(b), showing good agreement with the theoretical prediction following eq 7. It is worth noting that the proposed dielectric metasurface platform has a significantly increased differential transmittance as high as 89, demonstrating high sensitivity for chiral molecule detection.

CONCLUSION

We propose a dielectric metasurface consisting of achiral Ge nanoresonators, which provides high C enhancement in the mid-infrared range with a maximum value of more than 750, and the whole and central region volume-averaged C enhancement $C_{E\_ave\_whole}$ and $C_{E\_ave\_central}$ can reach about 148 and 215, respectively. We systematically investigated the effect of the parameters of the structure on the optical chirality enhancement. The metasurface successfully improves the CD signal of the deposited biolayer due to its strong superchiral field enhancement. It is found that the proposed dielectric metasurface has excellent performance, with the whole and central region volume-averaged C enhancement $C_{E\_ave\_whole\_bio}$ and $C_{E\_ave\_central\_bio}$ larger than 89 and 183 for a 50 nm thick chiral biolayer, respectively. Considering that the proposed metasurface is made of CMOS-compatible material Ge, they can be made by using standard semiconductor processes. For chiral sensing measurements, the analyte can be coated onto the metasurface and characterized by using a VCD spectrometer.[17] This work paves a novel route toward high-performance chiral sensing, enantioselectivity, and CD spectroscopy measurements in the mid-infrared range.

ASSOCIATED CONTENT

Supporting Information

The Supporting Information is available free of charge at https://pubs.acs.org/doi/10.1021/acsphotonics.3c01186.

S1: Approaching the generalized Kerker condition of the metasurface; S2: Spatial field distributions of the metasurface at the transmittance and reflectance intersection wavelengths; S3: Impact of tetramer nanoresonator parameters on the C enhancement of the metasurface; S4: Impact of sample imperfection and material absorption on the C enhancement of the metasurface coated with a biolayer; S5: Impact of Pasteur parameter κ and thickness of the chiral biolayer on the C enhancement of the metasurface (PDF)

AUTHOR INFORMATION

Corresponding Authors

Ming Lun Tseng − *Institute of Electronics, National Yang Ming Chiao Tung University, Hsinchu 300, Taiwan;* orcid.org/0000-0003-0418-8162; Email: mltseng@nycu.edu.tw

Hatice Altug − *Laboratory of Bionanophotonic Systems, Institute of Bioengineering, Ecole Polytechnique Fédérale de Lausanne (EPFL), Lausanne 1015, Switzerland;* orcid.org/0000-0001-5522-1343; Email: hatice.altug@epfl.ch

Authors

Longfang Ye − *Institute of Electromagnetics and Acoustics, School of Electronic Science and Engineering, Xiamen University, Xiamen 361005, People's Republic of China;* orcid.org/0000-0003-0867-6032

Jingyan Li − *Institute of Electromagnetics and Acoustics, School of Electronic Science and Engineering, Xiamen University, Xiamen 361005, People's Republic of China*

Felix Ulrich Richter − *Laboratory of Bionanophotonic Systems, Institute of Bioengineering, Ecole Polytechnique Fédérale de Lausanne (EPFL), Lausanne 1015, Switzerland*

https://doi.org/10.1021/acsphotonics.3c01186
ACS Photonics 2023, 10, 4377−4384

Yasaman Jahani − *Laboratory of Bionanophotonic Systems, Institute of Bioengineering, École Polytechnique Fédérale de Lausanne (EPFL), Lausanne 1015, Switzerland*

Rui Lu − *Jiangsu Key Laboratory of Chemical Pollution Control and Resources Reuse, School of Environmental and Biological Engineering, Nanjing University of Science and Technology, Nanjing 210094, People's Republic of China;* orcid.org/0000-0002-9666-480X

Bo Ray Lee − *Institute of Electronics, National Yang Ming Chiao Tung University, Hsinchu 300, Taiwan*

Complete contact information is available at: https://pubs.acs.org/10.1021/acsphotonics.3c01186

Notes

The authors declare no competing financial interest.

■ ACKNOWLEDGMENTS

L. Ye acknowledges the NSAF under Grant U2230118, Shenzhen Science and Technology Program under Grant JCYJ20210324121606017, and the Fundamental Research Funds for the Central Universities under Grant 20720210048, China. M. L. Tseng acknowledges the National Science and Technology Council (NSTC 112-2636-M-A49-001-) and the Ministry of Education (Yushan Fellow Program), Taiwan, and he is grateful to the support from the Center for Integrated Electronics-Optics Technologies and Systems, National Yang Ming Chiao Tung University. This work was also supported by the Higher Education Sprout Project of National Yang Ming Chiao Tung University and the Ministry of Education (MOE), Taiwan. This research has received funding from the European Innovation Council under grant agreement No. 10104642, TwistedNano funding under grant agreement No. 101046424, and the European Research Council (ERC) under grant agreement No. 682167 VIBRANT-BIO and 875672 POCSEL. We also acknowledge funding from the European Union Horizon 2020 Framework Programme for Research and Innovation under grant agreements No. FETOPEN-737071 (ULTRA-CHIRAL Project).

■ REFERENCES

(1) Barron, L. D. Chirality and Life. *Space Sci. Rev.* **2008**, *135* (1−4), 187−201.
(2) Yao, K.; Zheng, Y. Near-Ultraviolet Dielectric Metasurfaces: from Surface-Enhanced Circular Dichroism Spectroscopy to Polarization-Preserving Mirrors. *J. Phys. Chem.C* **2019**, *123* (18), 11814−11822.
(3) Cintas, P. On Chirality and the Universal Asymmetry. Reflections on Image and Mirror Image. Von Georges H. Wagnière. *Angew. Chem.* **2007**, *119* (48), 9303−9304.
(4) Cintas, P. The Origin of Chirality in the Molecules of Life. A Revision from Awareness to the Current Theories and Perspectives of this Unsolved Problem. Von Albert Guijarro und Miguel Yus. *Angew. Chem.* **2009**, *121* (12), 2113−2114.
(5) Pescitelli, G.; Woody, R. W. The exciton origin of the visible circular dichroism spectrum of bacteriorhodopsin. *J. Phys. Chem. B* **2012**, *116* (23), 6751−63.
(6) Tajmir-Riahi, H. A.; N'Soukpoé-Kossi, C. N.; Joly, D. Structural analysis of protein−DNA and protein−RNA interactions by FTIR, UV-visible and CD spectroscopic methods. *Spectroscopy* **2009**, *23* (2), 81−101.
(7) Shanmugam, G.; Polavarapu, P. L. Vibrational circular dichroism of protein films. *J. Am. Chem. Soc.* **2004**, *126* (33), 10292−5.
(8) Rogers, D. M.; Jasim, S. B.; Dyer, N. T.; Auvray, F.; Réfrégiers, M.; Hirst, J. D. Electronic Circular Dichroism Spectroscopy of Proteins. *Chem.* **2019**, *5* (11), 2751−2774.
(9) Bui, T. T. T.; Formaggio, F.; Crisma, M.; Monaco, V.; Toniolo, C.; Hussain, R.; Siligardi, G. TOAC: a useful Cα-tetrasubstituted α-amino acid for peptide conformational analysis by CD spectroscopy in the visible region. Part I. *J. Chem. Soc., Perkin Trans. 2* **2000**, No. 5, 1043−1046.
(10) Jeon, S.; Kim, S. J. Enhancement of Optical Chirality Using Metasurfaces for Enantiomer-Selective Molecular Sensing. *Appl. Sci.* **2021**, *11* (7), 2989.
(11) Morvan, M.; Mikšík, I. Recent Advances in Chiral Analysis of Proteins and Peptides. *Separations* **2021**, *8* (8), 112.
(12) Vazquez-Guardado, A.; Chanda, D. Superchiral Light Generation on Degenerate Achiral Surfaces. *Phys. Rev. Lett.* **2018**, *120* (13), No. 137601.
(13) Abdel-Megied, A. M.; Hanafi, R. S.; Aboul-Enein, H. Y. A chiral enantioseparation generic strategy for anti-Alzheimer and antifungal drugs by short end injection capillary electrophoresis using an experimental design approach. *Chirality* **2018**, *30* (2), 165−176.
(14) Agranat, I.; Caner, H.; Caldwell, J. Putting chirality to work: the strategy of chiral switches. *Nat. Rev. Drug Discovery* **2002**, *1* (10), 753−68.
(15) Nesterov, M. L.; Yin, X.; Schäferling, M.; Giessen, H.; Weiss, T. The Role of Plasmon-Generated Near Fields for Enhanced Circular Dichroism Spectroscopy. *ACS Photonics* **2016**, *3* (4), 578−583.
(16) Polavarapu, P. L.; He, J. T. Chiral analysis using Mid-IR vibrational CD spectroscopy. *Anal. Chem.* **2004**, *76* (3), 61a−67a.
(17) Kelly, S. M.; Jess, T. J.; Price, N. C. How to study proteins by circular dichroism. *Biochimica Et Biophysica Acta-Proteins and Proteomics* **2005**, *1751* (2), 119−139.
(18) Izumi, H.; Futamura, S.; Tokita, N.; Hamada, Y. Fliplike motion in the thalidomide dimer: Conformational analysis of (R)-thalidomide using vibrational circular dichroism spectroscopy. *J. Org. Chem.* **2007**, *72* (1), 277−279.
(19) Kurouski, D. Advances of Vibrational Circular Dichroism (VCD) in bioanalytical chemistry. A review. *Anal. Chim. Acta* **2017**, *990*, 54−66.
(20) Guo, C. N.; Shah, R. D.; Dukor, R. K.; Freedman, T. B.; Cao, X. L.; Nafie, L. A. Fourier transform vibrational circular dichroism from 800 to 10,000 cm(−1): Near-IR-VCD spectral standards for terpenes and related molecules. *Vib. Spectrosc.* **2006**, *42* (2), 254−272.
(21) Freedman, T. B.; Cao, X. L.; Dukor, R. K.; Nafie, L. A. Absolute configuration determination of chiral molecules in the solution state using vibrational circular dichroism. *Chirality* **2003**, *15* (9), 743−758.
(22) Hu, J.; Lawrence, M.; Dionne, J. A. High Quality Factor Dielectric Metasurfaces for Ultraviolet Circular Dichroism Spectroscopy. *ACS Photonics* **2020**, *7* (1), 36−42.
(23) Dong, L.; Yang, X.; Zhang, C.; Cerjan, B.; Zhou, L.; Tseng, M. L.; Zhang, Y.; Alabastri, A.; Nordlander, P.; Halas, N. J. Nanogapped Au Antennas for Ultrasensitive Surface-Enhanced Infrared Absorption Spectroscopy. *Nano Lett.* **2017**, *17* (9), 5768−5774.
(24) Tittl, A.; Leitis, A.; Liu, M.; Yesilkoy, F.; Choi, D. Y.; Neshev, D. N.; Kivshar, Y. S.; Altug, H. Imaging-based molecular barcoding with pixelated dielectric metasurfaces. *Science* **2018**, *360* (6393), 1105−1109.
(25) Rui, G.; Zou, S.; Gu, B.; Cui, Y. Surface-Enhanced Circular Dichroism by Localized Superchiral Hotspots in a Dielectric Dimer Array Metasurface. *J. Phys. Chem. C* **2022**, *126* (4), 2199−2206.
(26) Karawdeniya, B. I.; Damry, A. M.; Murugappan, K.; Manjunath, S.; Bandara, Y. M. N. D. Y.; Jackson, C. J.; Tricoli, A.; Neshev, D. Surface Functionalization and Texturing of Optical Metasurfaces for Sensing Applications. *Chem. Rev.* **2022**, *122* (19), 14990−15030.
(27) Luo, X. G.; Tsai, D. P.; Gu, M.; Hong, M. H. Extraordinary optical fields in nanostructures: from sub-diffraction-limited optics to sensing and energy conversion. *Chem. Soc. Rev.* **2019**, *48* (8), 2458−2494.
(28) Hassanfiroozi, A.; Yang, Z. S.; Huang, S. H.; Cheng, W. H.; Shi, Y. Z.; Wu, P. C. Vertically-Stacked Discrete Plasmonic Meta-Gratings

for Broadband Space-Variant Metasurfaces. *Advanced Optical Materials* **2023**, *11* (8), No. 2202717.
(29) Leitis, A.; Tseng, M. L.; John-Herpin, A.; Kivshar, Y. S.; Altug, H. Wafer-Scale Functional Metasurfaces for Mid-Infrared Photonics and Biosensing. *Adv. Mater.* **2021**, *33* (43), No. e2102232.
(30) García-Etxarri, A.; Dionne, J. A. Surface-enhanced circular dichroism spectroscopy mediated by nonchiral nanoantennas. *Phys. Rev. B* **2013**, *87* (23), No. 235409.
(31) Besteiro, L. V.; Zhang, H.; Plain, J.; Markovich, G.; Wang, Z.; Govorov, A. O. Aluminum Nanoparticles with Hot Spots for Plasmon-Induced Circular Dichroism of Chiral Molecules in the UV Spectral Interval. *Adv. Opt. Mater.* **2017**, *5* (16), No. 1700069.
(32) Vestler, D.; Shishkin, I.; Gurvitz, E. A.; Nasir, M. E.; Ben-Moshe, A.; Slobozhanyuk, A. P.; Krasavin, A. V.; Levi-Belenkova, T.; Shalin, A. S.; Ginzburg, P.; Markovich, G.; Zayats, A. V. Circular dichroism enhancement in plasmonic nanorod metamaterials. *Opt. Express* **2018**, *26* (14), 17841−17848.
(33) Lee, S.; Yoo, S.; Park, Q. H. Microscopic Origin of Surface-Enhanced Circular Dichroism. *ACS Photonics* **2017**, *4* (8), 2047−2052.
(34) Knipper, R.; Mayerhöfer, T. G.; Kopecký, V.; Huebner, U.; Popp, J. Observation of Giant Infrared Circular Dichroism in Plasmonic 2D-Metamaterial Arrays. *ACS Photonics* **2018**, *5* (4), 1176−1180.
(35) Mattioli, F.; Mazzeo, G.; Longhi, G.; Abbate, S.; Pellegrini, G.; Mogni, E.; Celebrano, M.; Finazzi, M.; Duò, L.; Zanchi, C. G.; Tommasini, M.; Pea, M.; Cibella, S.; Polito, R.; Sciortino, F.; Baldassarre, L.; Nucara, A.; Ortolani, M.; Biagioni, P. Plasmonic Superchiral Lattice Resonances in the Mid-Infrared. *ACS Photonics* **2020**, *7* (10), 2676−2681.
(36) Schäferling, M.; Yin, X.; Engheta, N.; Giessen, H. Helical Plasmonic Nanostructures as Prototypical Chiral Near-Field Sources. *ACS Photonics* **2014**, *1* (6), 530−537.
(37) Schäferling, M.; Engheta, N.; Giessen, H.; Weiss, T. Reducing the Complexity: Enantioselective Chiral Near-Fields by Diagonal Slit and Mirror Configuration. *ACS Photonics* **2016**, *3* (6), 1076−1084.
(38) Schäferling, M.; Dregely, D.; Hentschel, M.; Giessen, H. Tailoring Enhanced Optical Chirality: Design Principles for Chiral Plasmonic Nanostructures. *Phys. Rev. X* **2012**, *2* (3), No. 031010.
(39) Tseng, M. L.; Lin, Z. H.; Kuo, H. Y.; Huang, T. T.; Huang, Y. T.; Chung, T. L.; Chu, C. H.; Huang, J. S.; Tsai, D. P. Stress-Induced 3D Chiral Fractal Metasurface for Enhanced and Stabilized Broadband Near-Field Optical Chirality. *Adv. Opt. Mater.* **2019**, *7* (15), No. 1900617.
(40) Solomon, M. L.; Abendroth, J. M.; Poulikakos, L. V.; Hu, J.; Dionne, J. A. Fluorescence-Detected Circular Dichroism of a Chiral Molecular Monolayer with Dielectric Metasurfaces. *J. Am. Chem. Soc.* **2020**, *142* (43), 18304−18309.
(41) Zhao, X.; Reinhard, B. M. Switchable Chiroptical Hot-Spots in Silicon Nanodisk Dimers. *ACS Photonics* **2019**, *6* (8), 1981−1989.
(42) Du, K.; Li, P.; Wang, H.; Gao, K.; Liu, R. B.; Lu, F.; Zhang, W.; Mei, T. Optical Chirality Enhancement in Hollow Silicon Disk by Dipolar Interference. *Adv. Opt. Mater.* **2021**, *9* (5), No. 2001771.
(43) Ho, C.-S.; Garcia-Etxarri, A.; Zhao, Y.; Dionne, J. Enhancing Enantioselective Absorption Using Dielectric Nanospheres. *ACS Photonics* **2017**, *4* (2), 197−203.
(44) Mohammadi, E.; Tavakoli, A.; Dehkhoda, P.; Jahani, Y.; Tsakmakidis, K. L.; Tittl, A.; Altug, H. Accessible Superchiral Near-Fields Driven by Tailored Electric and Magnetic Resonances in All-Dielectric Nanostructures. *ACS Photonics* **2019**, *6* (8), 1939−1946.
(45) Mohammadi, E.; Tsakmakidis, K. L.; Askarpour, A. N.; Dehkhoda, P.; Tavakoli, A.; Altug, H. Nanophotonic Platforms for Enhanced Chiral Sensing. *ACS Photonics* **2018**, *5* (7), 2669−2675.
(46) Yao, K.; Liu, Y. Enhancing circular dichroism by chiral hotspots in silicon nanocube dimers. *Nanoscale* **2018**, *10* (18), 8779−8786.
(47) Solomon, M. L.; Hu, J.; Lawrence, M.; Garcia-Etxarri, A.; Dionne, J. A. Enantiospecific Optical Enhancement of Chiral Sensing and Separation with Dielectric Metasurfaces. *ACS Photonics* **2019**, *6* (1), 43−49.
(48) Solomon, M. L.; Saleh, A. A. E.; Poulikakos, L. V.; Abendroth, J. M.; Tadesse, L. F.; Dionne, J. A. Nanophotonic Platforms for Chiral Sensing and Separation. *Acc. Chem. Res.* **2020**, *53* (3), 588−598.
(49) Hassanfiroozi, A.; Cheng, Y.-C.; Huang, S.-H.; Lin, Y.-T.; Huang, P.-S.; Shi, Y.; Wu, P. C. Toroidal-Assisted Generalized Huygens' Sources for Highly Transmissive Plasmonic Metasurfaces. *Laser & Photonics Reviews* **2022**, *16* (6), No. 2100525.
(50) Gurvitz, E. A.; Ladutenko, K. S.; Dergachev, P. A.; Evlyukhin, A. B.; Miroshnichenko, A. E.; Shalin, A. S. The High-Order Toroidal Moments and Anapole States in All-Dielectric Photonics. *Laser & Photonics Reviews* **2019**, *13*, No. 1800266.
(51) Graf, F.; Feis, J.; Garcia-Santiago, X.; Wegener, M.; Rockstuhl, C.; Fernandez-Corbaton, I. Achiral, Helicity Preserving, and Resonant Structures for Enhanced Sensing of Chiral Molecules. *ACS Photonics* **2019**, *6* (2), 482−491.
(52) Garcia-Guirado, J.; Svedendahl, M.; Puigdollers, J.; Quidant, R. Enhanced Chiral Sensing with Dielectric Nanoresonators. *Nano Lett.* **2020**, *20* (1), 585−591.

https://doi.org/10.1021/acsphotonics.3c01186
ACS Photonics 2023, 10, 4377−4384